



## Article

# Facile Fabrication of Wood-Derived Porous Fe<sub>3</sub>C/Nitrogen-Doped Carbon Membrane for Colorimetric Sensing of Ascorbic Acid

Sadaf Saeedi Garakani <sup>1</sup>, Miao Zhang <sup>1</sup>, Dongjiu Xie <sup>2</sup>, Anirban Sikdar <sup>1</sup>, Kanglei Pang <sup>1</sup> and Jiayin Yuan <sup>1,\*</sup>

- <sup>1</sup> Department of Materials and Environmental Chemistry, Stockholm University, 10691 Stockholm, Sweden; sadaf.saeedigarakani@mmk.su.se (S.S.G.); miao.zhang@mmk.su.se (M.Z.); anirban.sikdar@mmk.su.se (A.S.); kanglei.pang@mmk.su.se (K.P.)
- <sup>2</sup> Department for Electrochemical Energy Storage, Helmholtz-Zentrum Berlin für Materialien und Energie, Hahn-Meitner Platz 1, 14109 Berlin, Germany; dongjiu.xie@helmholtz-berlin.de
- \* Correspondence: jiayin.yuan@mmk.su.se

**Abstract:** Fe<sub>3</sub>C nanoparticles hold promise as catalysts and nanozymes, but their low activity and complex preparation have hindered their use. Herein, this study presents a synthetic alternative toward efficient, durable, and recyclable, Fe<sub>3</sub>C-nanoparticle-encapsulated nitrogen-doped hierarchically porous carbon membranes (Fe<sub>3</sub>C/N-C). By employing a simple one-step synthetic method, we utilized wood as a renewable and environmentally friendly carbon precursor, coupled with poly(ionic liquids) as a nitrogen and iron source. This innovative strategy offers sustainable, high-performance catalysts with improved stability and reusability. The Fe<sub>3</sub>C/N-C exhibits an outstanding peroxidase-like catalytic activity toward the oxidation of 3,3',5,5'-tetramethylbenzidine in the presence of hydrogen peroxide, which stems from well-dispersed, small Fe<sub>3</sub>C nanoparticles jointly with the structurally unique micro-/macroporous N-C membrane. Owing to the remarkable catalytic activity for mimicking peroxidase, an efficient and sensitive colorimetric method for detecting ascorbic acid over a broad concentration range with a low limit of detection (~2.64 μM), as well as superior selectivity, and anti-interference capability has been developed. This study offers a widely adaptable and sustainable way to synthesize an Fe<sub>3</sub>C/N-C membrane as an easy-to-handle, convenient, and recoverable biomimetic enzyme with excellent catalytic performance, providing a convenient and sensitive colorimetric technique for potential applications in medicine, biosensing, and environmental fields.

**Keywords:** iron carbide nanoparticles; nitrogen-doped carbon; wood-derived carbon; colorimetric detection; ascorbic acid



**Citation:** Saeedi Garakani, S.; Zhang, M.; Xie, D.; Sikdar, A.; Pang, K.; Yuan, J. Facile Fabrication of Wood-Derived Porous Fe<sub>3</sub>C/Nitrogen-Doped Carbon Membrane for Colorimetric Sensing of Ascorbic Acid. *Nanomaterials* **2023**, *13*, 2786. <https://doi.org/10.3390/nano13202786>

Academic Editors: Christian Kramberger, Alexander Chernov and Marianna Kharlamova

Received: 26 September 2023

Revised: 11 October 2023

Accepted: 12 October 2023

Published: 18 October 2023



**Copyright:** © 2023 by the authors. Licensee MDPI, Basel, Switzerland. This article is an open access article distributed under the terms and conditions of the Creative Commons Attribution (CC BY) license (<https://creativecommons.org/licenses/by/4.0/>).

## 1. Introduction

Ascorbic acid (AA), also called vitamin C, is a crucial water-soluble vitamin. Its antioxidant properties are effective for developing the immune system, preventing and treating some diseases such as cancer, and creating collagen in various tissues in the human body [1,2]. Since the human body cannot generate this vital vitamin, gaining enough AA from the daily diet and health supplements is essential. Consequently, developing quick and straightforward approaches to determine the concentration of AA with high selectivity and accuracy is required in different fields, e.g., pharmacy and food industries [3]. So far, several methods, for instance, high-performance liquid chromatography (HPLC) [4], capillary electrophoresis [5], fluorescence [6], and electrochemistry [7], have been used to evaluate the AA concentration. Compared with other techniques, the colorimetric assay has recently gained widespread attention as a reliable biosensor due to its distinctive advantages such as rapid detection, simplicity, superb sensitivity, low cost, and facile optical detection with the naked eye [8]. To develop a quick colorimetric sensor, peroxidase, a

kind of natural enzyme, plays a pivotal role thanks to its high catalytic efficiency and specificity [9]. However, high cost, low stability, brief shelf life, and harsh environmental conditions significantly hamper its practical use [10]. To overcome these challenges, researchers have developed nanomaterial-based artificial enzymes (“nanozymes”) that can mimic the functions of natural enzymes [11]. So far, a collection of nanomaterials, e.g., metallic nanoparticles [12,13], carbon-based nanomaterials [14,15], and metal–organic frameworks (MOFs) [16], have been successfully crafted, which demonstrated the inherent peroxidase-like function.

Recently, Fe<sub>3</sub>C, a member of the iron carbide family, indicated outstanding peroxidase-like catalytic activity because of its high redox capacity, a large number of active sites, and superior surface reactivity [17,18]. Especially, the ultrafine Fe<sub>3</sub>C-based nanoparticles possess highly exposing active sites and could therefore be considered as a promising catalytic agent. Nevertheless, the strong aggregation tendency of Fe<sub>3</sub>C nanoparticles often leads to loss of surface area, reducing their catalytic capacity [19,20]. Dispersing Fe<sub>3</sub>C nanoparticles over a porous conducting matrix, especially heteroatom-doped porous conductive carbon, could be an effective strategy to minimize nanoparticle aggregation. In this composite catalyst, the carbon matrix plays a dual role: first, it maintains the high catalytically active surface area for Fe<sub>3</sub>C; second, it endows the catalyst with sufficient conductivity and chemical stability due to the carbon component [21,22]. In addition, the heteroatom doping of carbon may synergistically boost the catalytic process through tuning the local electronic and chemical structure [23]. Therefore, it is of high interest to explore synthetic strategies to synthesize ultrafine Fe<sub>3</sub>C nanoparticles dispersed over a heteroatom-doped porous carbon matrix that can exhibit peroxidase-like activity.

Herein, we established a facile wood-based method for synthesizing a nitrogen-doped porous carbon membrane containing well-dispersed Fe<sub>3</sub>C nanoparticles (termed “Fe<sub>3</sub>C/N–C”) through sequential pyrolytic treatments. The as-prepared Fe<sub>3</sub>C/N–C catalyst illustrated an excellent characteristic peroxidase-like activity to 3,3',5,5'-tetramethylbenzidine (TMB) oxidation due to the ultrafine Fe<sub>3</sub>C nanoparticles and their corresponding cooperative interfacial effect between Fe<sub>3</sub>C nanoparticles and the nitrogen-doped carbon matrix. Because of the elevated catalytic activity, a convenient colorimetric assay of AA has been developed. It has been proven that the optimized Fe<sub>3</sub>C/N–C composite catalysts are impressive peroxidase mimics, which exhibit promising opportunities in the fields of biosensors and biomedicine.

## 2. Experimental Section

**Materials.** Balsa wood was purchased from Material AB, Sweden. 1-Vinylimidazole (99%) and sodium tetrafluoroborate were obtained from Alfa Aesar, Karlsruhe, Germany. Potassium hexafluorophosphate was purchased from Acros Organics, France. Bromoacetonitrile (95%) was purchased from TCI, Europe. Lithium bis(trifluoromethane sulfonyl)imide (LiTFSI, 99.95%) was purchased from Io-li-tec, Heilbronn, Germany. Sodium chlorite, sodium acetate, 3,3',5,5'-tetramethyl-benzidine (TMB), L-ascorbic acid, and iron (III) chloride were purchased from Sigma-Aldrich, Darmstadt, Germany. N,N-dimethylformamide (DMF) was obtained from Honeywell, Germany. H<sub>2</sub>O<sub>2</sub> was purchased from VWR, Leuven, Belgium. All chemicals were used without any further purification. Solvents were of analytical grade.

**Poly(ionic liquid) (PIL) synthesis.** The polymer precursor with Br<sup>−</sup> as counteranion, poly(1-cyanomethyl-3-vinylimidazolium bromide) (PCMVImBr), was synthesized in reference to our earlier published procedure [24]. Its chemical structure was characterized through proton nuclear magnetic resonance (<sup>1</sup>H-NMR) spectroscopy, as demonstrated in Figure S1. Poly(1-cyanomethyl-3-vinylimidazolium bis(trifluoromethane sulfonyl)imide) (PCMVImTFSI) was made through an anion metathesis reaction between PCMVImBr and LiTFSI in their aqueous solution. In a standard anion-exchange procedure, an aqueous solution of LiTFSI was added dropwise to an aqueous solution of PCMVImBr at a concentration of 1 wt%. The final TFSI/Br molar ratio was set as 1.15/1. The precipitate was

filtered off and washed with pure water several times, and finally dried at 70 °C under vacuum until constant weight.

**Wood delignification.** Balsa wood with a density of 123 kg m<sup>-3</sup> was sliced into thin membranes with controllable thickness using cutting equipment (secotom-50). The cutting direction was maintained perpendicular to the growth direction of the trunk. Before chemical treatment, all wood slices were dried at 80 °C in an oven for 10 h. To extract hemicellulose and lignin, a well-established method was employed using sodium chlorite (1 wt%) with acetate buffer solution (pH 4.6) for 6 h at 80 °C. After the treatment, the membranes were rinsed with deionized water and ethanol and dried at room temperature until constant weight.

**Preparation of the Fe<sub>3</sub>C/N-C catalyst.** Amounts of 0.200 g of the as-synthesized PCMVImTFSI and 0.030 g of iron (III) chloride were thoroughly dissolved in 2 mL of DMF until a homogenous solution was achieved. The 0.600 g delignified wood membranes were coated with the solution and dried at 80 °C for 2 h. The obtained membranes were immersed in a 0.25 wt% aqueous ammonia solution for 2 h to generate a porous polymeric structure on the cells of the wood. Then, the obtained membranes were washed with pure water several times. It was finally dried under ambient conditions until a constant weight. Next, the prepared membranes were carbonized as the following procedure in a tube furnace. First, the membranes were heated at 300 °C in nitrogen flow for 1 h, heated to 600 °C, and maintained at this temperature for 1 h; finally, they were heated to 900 °C and kept for 10 min. For comparison, the membrane was also carbonized at different final temperatures, including 700, 800, and 1000 °C. Finally, the Fe<sub>3</sub>C/N-C catalysts were obtained.

**Peroxide catalytic activity.** Typically, 20 µL of the as-prepared Fe<sub>3</sub>C/N-C suspension (3 mg mL<sup>-1</sup>) and 20 µL of TMB solution (15 mM) in DMSO were added into 3 mL of acetate buffer solution (pH 4) containing H<sub>2</sub>O<sub>2</sub> (50 mM) at room temperature. The oxidation of TMB by the catalyst was studied by monitoring the absorbance peak at 652 nm after 10 min of reaction. The other groups, including TMB + H<sub>2</sub>O<sub>2</sub> and TMB + catalyst (Fe<sub>3</sub>C/N-C) at the same concentration as mentioned, were selected as the controls. Photographs of the reaction solution were obtained, and UV-Vis absorbance was collected using a UV-Vis-NIR spectrophotometer (Agilent Technologies, Santa Clara, CA, USA). Under the above-mentioned concentrations, the catalyst's pH tolerance was investigated in a wide range (2.0–11.0) at room temperature. Similarly, temperature tolerance was examined in the reaction by altering the temperature between 25 and 60 °C in acetate buffer (pH 4).

**Kinetic analysis.** The kinetics of the reaction was considered by monitoring the absorbance variation at 652 nm at one-minute intervals in a scanning mode. The steady-state kinetics was analyzed using H<sub>2</sub>O<sub>2</sub> and TMB as substrates. The tests were performed by altering the TMB concentration at a fixed H<sub>2</sub>O<sub>2</sub> concentration or contrariwise. The Michaelis–Menten equation was applied to determine the kinetic parameters (Equation (1)).

$$\text{Michaelis–Menten } v = V_{max} \times [S] / (K_m + [S]) \quad (1)$$

where  $v$ ,  $V_{max}$ ,  $[S]$ , and  $K_m$  represent the initial velocity, maximum reaction velocity, substrate concentration, and Michaelis constant, respectively. The molar attenuation coefficient of TMB at 652 nm was 39,000 M<sup>-1</sup>cm<sup>-1</sup>. The tests were carried out in a colorimetric dish of 1 cm in thickness.

**Detection of ascorbic acid.** AA detection was studied as follows: 15 µL of H<sub>2</sub>O<sub>2</sub> sample, 60 µL of TMB solution, and 20 µL of catalyst dispersion in acetate buffer (pH 4.0) with a final volume 500 µL reacted for 15 min at room temperature, and the blue color of oxTMB was observed. Then, the ascorbic acid samples at different concentrations of 0–200 µM were individually added to the blue solution, and the UV-Vis absorbance at 652 nm was monitored. Similarly, the experiment was repeated by replacing AA with various reagents such as sulfite, citric acid, glycine, serine, alanine, aspartic acid, tartaric acid, arginine, and saccharides like glucose, lactose, and fructose.

**Characterization.** Phase structure was examined on an X-ray diffractometer PANalytical X'Pert Pro (Malvern Instruments, Malvern, UK) applying Cu K $\alpha$  radiation ( $\lambda = 1.5418 \text{ \AA}$ ) between  $5^\circ$  and  $80^\circ$  at a scan rate of  $0.2^\circ/\text{min}$ . Chemical bonding characterizations were monitored through ESCALAB 250Xi X-ray photoelectron spectroscopy (XPS) (USA). The morphology of samples was investigated using a JEOL 7000F (JEOL Ltd., Tokyo, Japan) scanning electron microscope (SEM) operated at 10 kV. Samples were sputtered by a thin gold layer for 60 s before the examination. Energy-dispersive X-ray (EDX) mapping was taken on the SEM using an EDX spectrometer. The particle size was determined through transmission electron microscopy (TEM) using a JEOL JEM-2100 (JEOL GmbH, Eching, Germany) operated at 200 kV. The nitrogen sorption isotherms at 77 K were performed using the Micromeritics ASAP 2020 (Accelerated Surface Area and Porosimetry system, Germany). Before the sorption experiments, all samples were degassed for 7 h at 373 K under vacuum. The Brunauer–Emmett–Teller (BET) equation was used to calculate the specific surface area. Thermogravimetric analysis (TGA) experiments were carried out at a heating rate of  $10^\circ\text{C min}^{-1}$  from  $50^\circ\text{C}$  to  $900^\circ\text{C}$  under air flow using a TA Instruments Discovery TG. Raman spectroscopy was performed on a Horiba Labram HR system with 532 nm laser excitation.  $^1\text{H-NMR}$  spectra were performed at room temperature using a Bruker DPX-400 spectrometer operating at 400 MHz. DMSO- $d_6$  was employed as an NMR solvent for the measurement. Additionally, the catalytic attributes were examined through ultraviolet-visible (UV-Vis, Agilent Technologies UV-Vis-NIR spectrophotometer, Petaling Jaya, Malaysia) measurement.

### 3. Results and Discussion

$\text{Fe}_3\text{C}$  nanoparticle-functionalized nitrogen-doped porous carbon membranes, termed  $\text{Fe}_3\text{C/N-C}$ , were synthesized via a facile pyrolysis of Balsa wood in the presence of a mixture of poly(ionic liquid) and  $\text{FeCl}_3$  as N/Fe sources. It is known that the chemical nature and microstructure of precursors strongly affect the physiochemical properties and chemical composition of heteroatom-doped carbon products [25]. Thus, wood carrying the elegant form of interconnected and oriented channel-like pores, in addition to its renewability and low cost, stands out as an attractive source for conductive porous carbon matrix [26,27]. Obviously, various types of wood possess different internal porous structures, and Balsa wood was chosen here as a carbon precursor owing to its multi-channel hierarchically porous structure. Furthermore, due to its high nitrogen content, poly(ionic liquid) (PIL) as the polymerization product of ionic liquids can serve as the source of nitrogen that endows porous carbons with target N doping; in addition, the PIL can induce the formation of extra porous carbon structures through its catalytic degradation of biomass [28]. In comparison to other types of polymers, PILs can be more thermally stable to secure a high carbonization yield [29,30], can be rich in heteroatoms of different types that can dope carbon products [31,32], and can molecularly disperse the iron precursor to secure uniform formation of  $\text{Fe}_3\text{C}$  nanoparticles in the porous carbon matrix [33]. To note, the cation–anion pair in PIL is one of the key parameters in creating the tiny pores to accommodate active sites for catalysis [24]. Using the wood slice and PIL as precursors readily enables the formation of a thin porous carbon membrane, which is effective for the enrichment of AA and proper for practical use in in situ detection. More significantly, as a heterogeneous catalyst at a macroscopic size, the composite membrane can be recycled at will from the liquid reaction system [34,35].

In a typical synthetic run, after chemical treatment of Balsa wood to remove lignin and hemicellulose, a mixture of an aqueous solution of  $\text{FeCl}_3$  and PCMVImTFSI (TFSI denotes the counteranion) was coated onto the wood cells' surface through straightforward wet-impregnation and drying under ambient conditions to constant weight. PILs are well known for their high surface activities and attach themselves efficiently onto the wood surface via multiple intermolecular interactions, e.g., hydrogen bonding and van der Waals interaction. Because of the ionic complexation of the iron cation with the -CN unit and the ion pair in the PIL, the  $\text{FeCl}_3$  can be embedded in PIL and uniformly anchor as a coating

layer onto the porous wood surface [36]. This step is critical for forming the iron carbide nanoparticles and minimizing their severe aggregation caused by the uneven distribution of iron precursors. Afterward, a pyrolysis treatment at various carbonization temperatures under nitrogen was performed to generate the target  $\text{Fe}_3\text{C}/\text{N}-\text{C}$  membranes.

Because of the benefit of the facile scalable synthetic method, the technique can properly tailor the hierarchical membrane with a controllable composition and microstructure. Since the enzyme-mimicking activities of carbon materials are obviously affected by the final carbonization temperatures, the alteration in catalytic activity against the carbonization temperature was studied first between 700 °C and 1000 °C, wherein 900 °C was identified as the optimum temperature; thus, studies thereafter were based on this sample (Figure S2). As shown in the inset of Figure 1a, a photograph of a spherical carbon membrane of  $\text{Fe}_3\text{C}/\text{N}-\text{C}$  of 1 cm in diameter is presented. Since the  $\text{Fe}_3\text{C}/\text{N}-\text{C}$  membrane is cuttable by a normal cutter, it can be easily produced in different sizes and shapes. Next, the morphology of the as-synthesized catalyst was studied using scanning electron microscopy (SEM) and transmission electron microscopy (TEM). The cross-sectional SEM images of  $\text{Fe}_3\text{C}/\text{N}-\text{C}$  (Figure 1a,b and Figure S3) show that the 3D porous structure of the Balsa wood with well-aligned microchannels are completely preserved after the pyrolysis process [37]. This open channel in the 3D porous carbon framework with low tortuosity can significantly lower the diffusion length, resulting in smooth and fast mass transportation to and from the active sites [38]. Besides the large-sized channels, the SEM images further reveal the presence of macropores of  $1.75 \pm 0.5 \mu\text{m}$  sitting directly on the cell wall of the carbon, which interconnect parallel channels of the carbon framework.

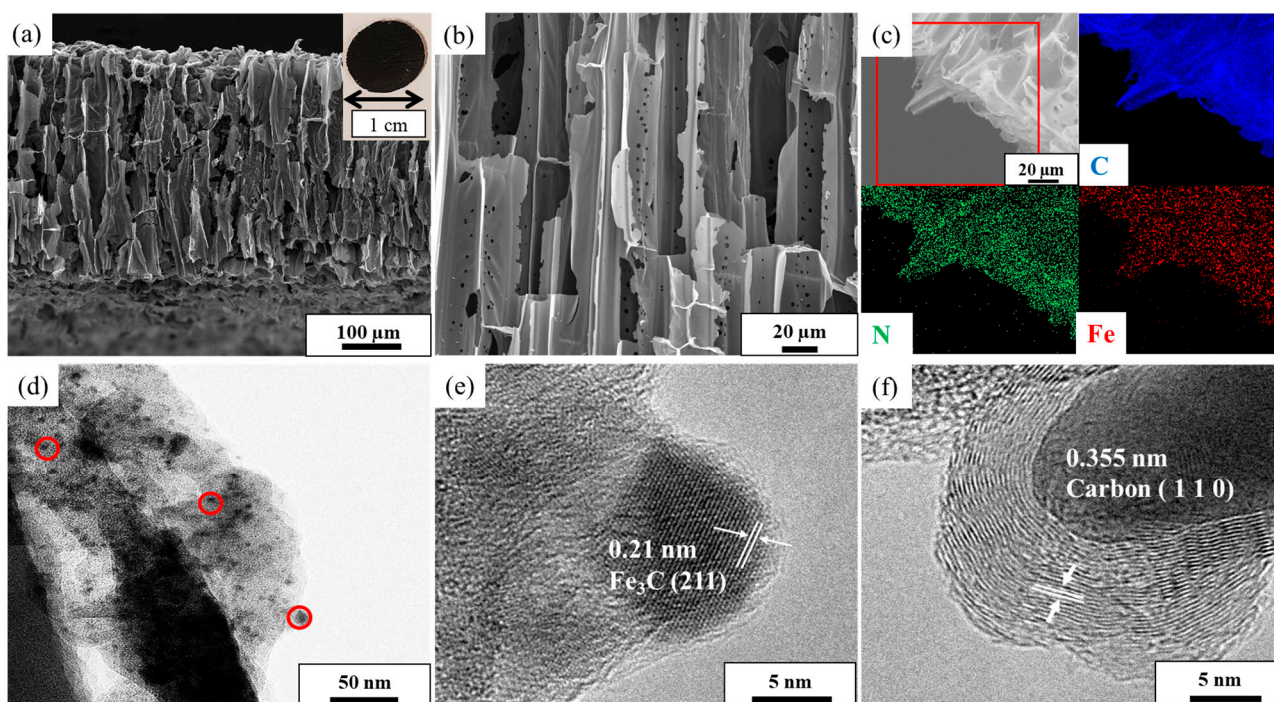


**Figure 1.** (a,b) Cross-sectional SEM images of  $\text{Fe}_3\text{C}/\text{N}-\text{C}$ , respectively. The inset in (a) shows the photograph of the final membrane prepared at 900 °C. (c) Elemental mapping of different elements in  $\text{Fe}_3\text{C}/\text{N}-\text{C}$ , (d) TEM image of  $\text{Fe}_3\text{C}/\text{N}-\text{C}$ , and (e,f) HR-TEM images of  $\text{Fe}_3\text{C}/\text{N}-\text{C}$ .

The decoration of  $\text{Fe}_3\text{C}$  nanoparticles over the porous carbon framework was revealed by TEM images. Figure 1d displays nanoparticles of  $\text{Fe}_3\text{C}$  homogeneously dispersed over the thin carbon nanosheets without agglomeration. Importantly, the histogram of the nanoparticles' size distribution (Figure S4) shows that the average diameter of the  $\text{Fe}_3\text{C}$  nanoparticles is small,  $4.9 \pm 2.5 \text{ nm}$ . The ultra-small nanoparticles embedded in the porous carbons possess rich accessible active sites and therefore are beneficial to their catalytic

performance [39]. To study the role of PIL on the formation of dispersed  $\text{Fe}_3\text{C}$  nanoparticles, a control sample was synthesized without PIL under the same condition. The TEM image of the control sample demonstrates the aggregation of nanoparticles into a large size of  $39 \pm 19$  nm (Figures S5 and S6), confirming the cooperative role of PIL in the formation of well-dispersed  $\text{Fe}_3\text{C}$  nanoparticles. To further analyze the successful formation of the  $\text{Fe}_3\text{C}/\text{N-C}$  catalyst, we switched to energy-dispersive X-ray (EDX) mapping and high-resolution TEM (HR-TEM) images. First, the EDX mapping shows the microscopic uniform distribution of Fe, N, and C elements across the catalyst surface (Figure 1c), in accordance with the observed homogenous distribution of  $\text{Fe}_3\text{C}$  nanoparticles within the porous carbons through TEM. The presence of the N element supports the successful doping of the carbon framework with nitrogen atoms owing to the decomposition and doping of the carbon matrix by PIL at high temperature ( $>500$  °C) [40]. From the HR-TEM images of  $\text{Fe}_3\text{C}/\text{N-C}$  (Figure 1e,f), we can clearly observe two distinct crystalline phases with lattice spacings of 0.21 nm and 0.36 nm corresponding to the crystallographic planes (220) of  $\text{Fe}_3\text{C}$  and (002) of graphitic carbon, respectively [41,42]. The presence of a graphitic phase (002) with an interlayer spacing of 0.36 nm suggests the occurrence of a graphitization process of the wood/PIL mixture at a temperature of 900 °C due to the catalytic role of PIL to biomass during pyrolysis [28].

The degree of graphitization and the phase structure information of the carbons in  $\text{Fe}_3\text{C}/\text{N-C}$  were studied using Raman spectroscopy. Figure 2a shows the appearance of two distinct bands at  $1350\text{ cm}^{-1}$  and at  $1590\text{ cm}^{-1}$ , which are assigned, respectively, to the D-band originating from the disorder in carbon atoms and structural defects, and the G-band, which is attributed to the ordered carbon structures [31,43]. The intensity ratio of the D band to the G band was quantitatively calculated to be 0.98. Importantly, graphitization improves the transport of electrons through the carbonized porous wood, which for this sample is measured to be  $232 \pm 16$  S/m as the apparent conductivity (due to the presence of pores). As a result, this graphitic wood could serve as a conductive matrix to favor peroxidase catalytic activity.

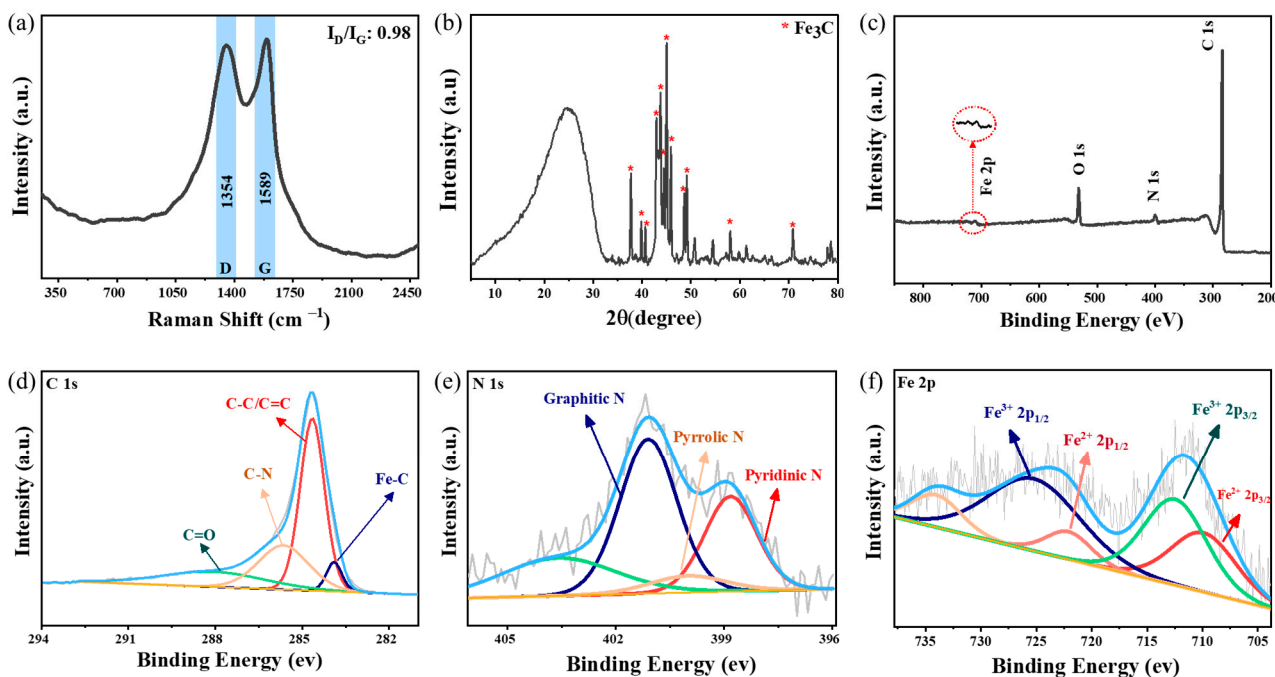


**Figure 2.** (a) Raman spectrum, (b) XRD pattern, and (c) XPS full survey spectrum of the obtained  $\text{Fe}_3\text{C}/\text{N-C}$ ; (d–f) XPS survey spectra of C 1s, N 1s, and Fe 2p, respectively.

The phase structure of as-synthesized  $\text{Fe}_3\text{C}/\text{N-C}$  catalysts was analyzed via an X-ray diffraction (XRD) study. In Figure 2b, the diffraction peaks at  $25.0^\circ$ ,  $42.9^\circ$ ,  $44.4^\circ$ ,  $54.4^\circ$ , and

77.9° could be assigned to the diffraction planes of (002), (100), (101), (004), and (110) of the graphitic phase (JCPDS: 41-1487), respectively. The diffraction peaks at 37.7°, 39.8°, 40.6°, 42.8°, 43.8°, 44.5°, 45.0°, 45.9°, 48.6°, and 49.1° can be attributed to the crystal planes of (210), (002), (201), (211), (102), (220), (031), (112), (131), and (221) of the Fe<sub>3</sub>C phase (JCPDS 35-0772), respectively. The iron content of the Fe<sub>3</sub>C/N-C was analyzed through thermogravimetric analysis (TGA) (Figure S7). After aerobic pyrolysis of Fe<sub>3</sub>C/N-C, as expected, the residue was identified as Fe<sub>2</sub>O<sub>3</sub> (Figure S8). As shown in Figure S4, based on the iron oxide mass after the TGA test (3.83 wt%), the iron content of the Fe<sub>3</sub>C/N-C was calculated as 2.8 wt%.

We further analyzed the sample through X-ray photoelectron spectroscopy (XPS) to understand the surface chemical composition and the electronic state of the elements in the Fe<sub>3</sub>C/N-C catalyst. From the survey spectrum of the Fe<sub>3</sub>C/N-C (Figure 2c), we can confirm the presence of C, N, O, and Fe elements, as expected [44]. The survey spectrum further reveals the presence of 3.65 atom% and 1.02 atom% of N and Fe, respectively, on the surface. The compound content calculated from XPS is lower than the actual amount, which can be attributed to the fact that XPS analysis has restricted access to the iron carbide nanoparticles and nitrogen atoms embedded inside the carbon layers due to the limited detecting depth in XPS (~5 nm) [45,46]. The high-resolution C 1s spectrum (Figure 2d) was fitted with four peaks corresponding to C-Fe (283.9 eV), C-C/C=C (284.6 eV), C-N (285.6), and C=O (288.0 eV) [47,48], suggesting the existence of graphite-like carbon (in an abundance of 50 atom%), nitrogen binding carbon (C-N), and iron binding carbon (Fe-C). Figure 2e shows the N 1s spectrum, which can be deconvoluted into four peaks, corresponding to the pyridinic N (398.8 eV), pyrrolic N (400 eV), graphitic N (401.1 eV), and oxidized-N (403.6), verifying the N-doping nature of the carbon structure [49,50]. It is worth mentioning that graphitic N sites (which, in our case, is around 45 atom%) particularly have the capability to improve the circulation of electrons due to their smaller diameter and higher electronegativity than carbon atoms [51]. Hence, graphitic carbon plus a significant amount of graphitic N in the network can combine together and encourage the breakage of the O-O bond in hydrogen peroxide [52]. As displayed in Figure 2f, the high-resolution Fe 2p XPS spectrum reveals two characteristic Fe 2p<sub>3/2</sub> and Fe 2p<sub>1/2</sub> peaks. The deconvoluted Fe 2p spectrum with peak positions at Fe<sup>2+</sup> 2p<sub>3/2</sub> (709.9 eV), Fe<sup>3+</sup> 2p<sub>3/2</sub> (712.5 eV), Fe<sup>2+</sup> 2p<sub>1/2</sub> (722.0 eV), and Fe<sup>3+</sup> 2p<sub>1/2</sub> (725.2 eV) demonstrates the successful formation of Fe<sub>3</sub>C over the porous carbon framework [53,54].

Generally speaking, surface area and porous structure play a crucial role in catalysis [55]. With the other conditions being the same, samples with a higher surface area show better catalytic performance [9,56]. The surface area and pore size distribution were studied through the nitrogen sorption isotherm (Figure S9). The isotherm exhibited an IUPAC-type IV shape. The specific surface area ( $S_{\text{BET}}$ ) and pore volume of Fe<sub>3</sub>C/N-C were 327 m<sup>2</sup> g<sup>-1</sup> and 0.17 cm<sup>3</sup> g<sup>-1</sup>, respectively. Furthermore, Figure S10 displays the pore size distribution plot and proves the existence of dominant micropores and small mesopores [57]. The abundant microporous structure, if accessible, is vital to improving the catalytic activity because they can host the compact catalytic sites owing to the high surface-to-volume ratio [58–60]. Nevertheless, it is challenging for rich micropores in the membrane to exert their entire catalytic capacity due to the large diffusion resistance through pores below 2 nm in size. This challenge can be effectively addressed by the presence of mesopores, as shown in Figure S10, and macropores, as proven by the SEM image. Such a hierarchy in pores is valuable for catalysis, as micropores with rich active sites can be connected to meso- and/or macropores to balance the catalytic activity and mass transfer kinetics [36,61].

**Mimetic peroxidase activity.** According to previous studies, carbon materials containing iron and nitrogen species illustrated enzyme-like catalytic properties [62,63]. For biosensors and other analytical applications, the optical properties of the sample were first monitored and investigated. The peroxidase-like activity of Fe<sub>3</sub>C/N-C was evaluated in the oxidation reaction of TMB in the presence of H<sub>2</sub>O<sub>2</sub>. In a typical process, the colorless liquid reaction mixture becomes blue with a characteristic absorbance peak emerging at

652 nm, originating from the oxidized TMB (termed ox-TMB), similar to what has been observed for the well-known horseradish peroxidase (HRP) [64,65]. The TMB solution, which only contained either  $H_2O_2$  or the catalyst of  $Fe_3C/N-C$ , did not show a distinguishable UV-Vis adsorbance at 652 nm, and the reaction system remained colorless and unchanged (curves and inset in Figure 3a). These results suggested that the oxidation reaction did not take place. Once the catalyst,  $H_2O_2$ , and TMB were all combined in the system, the blue color emerged (curve and inset A1 in Figure 3a). This proved that the  $Fe_3C/N-C$  could decompose  $H_2O_2$ , which is responsible for triggering the oxidation reaction of TMB into ox-TMB that showed up as an absorption peak at 652 nm in the UV-Vis spectrum [66,67].

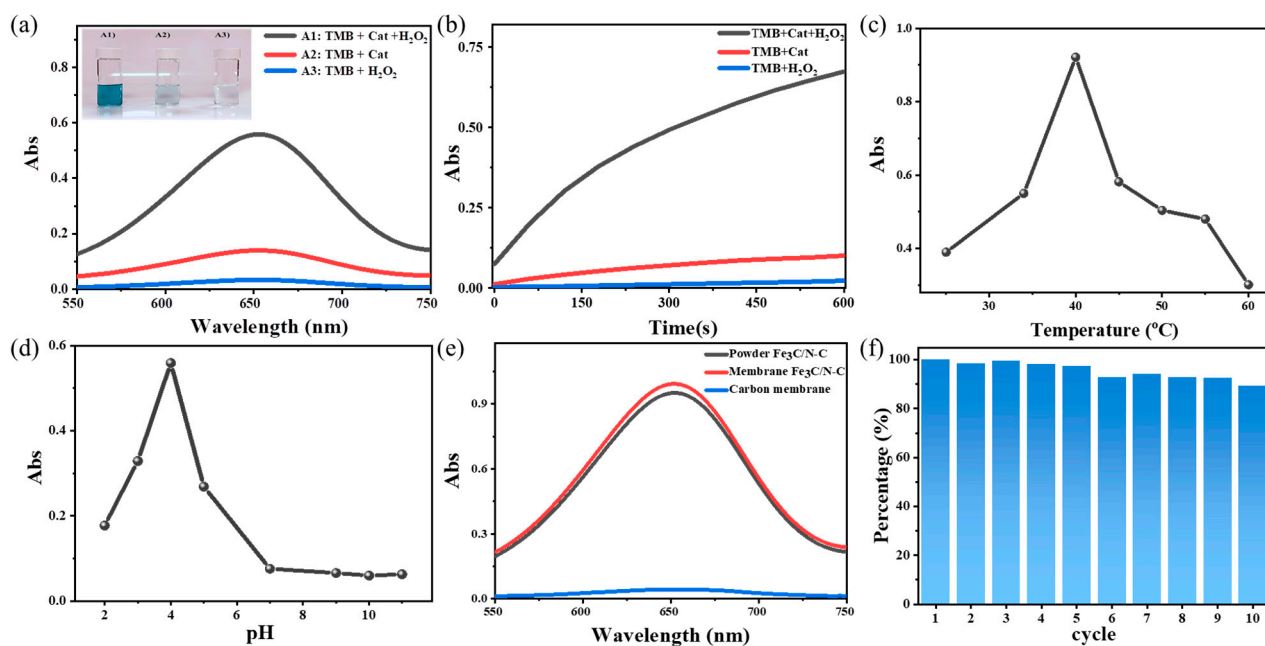


**Figure 3.** (a) UV-Vis absorbance and the corresponding optical photographs of the ox-TMB recorded in three systems (TMB +  $H_2O_2$ , TMB + Cat, TMB +  $H_2O_2$  + Cat) in acetate buffer solutions at a pH value of 4.0. (b) Time-dependent absorbance spectra of ox-TMB at 652 nm in the three systems (TMB +  $H_2O_2$ , TMB + Cat, TMB +  $H_2O_2$  + Cat). (c,d) Dependence of the peroxidase-like activity of the obtained  $Fe_3C/N-C$  catalyst with varied temperature and pH values, respectively. (e) UV-Vis absorbance of the ox-TMB recorded with three catalysts (powder  $Fe_3C/N-C$ , membrane  $Fe_3C/N-C$ , pure carbon membrane) in acetate buffer solutions at a pH value of 4.0. (f) The stability test of the catalyst after 10 cycles of use.

Several parameters, such as reaction time, pH, temperature, and the concentration of  $H_2O_2$  and TMB, could affect the catalytic performance of  $Fe_3C/N-C$  [11]. Figure 3b reveals the intensity of the absorbance peak at 652 nm of the mixtures of TMB + Cat ( $Fe_3C/N-C$ ), TMB +  $H_2O_2$ , and TMB +  $H_2O_2$  + Cat systems after a reaction period of 10 min. The significant and continuous alteration in absorbance was detected in the TMB +  $H_2O_2$  + Cat system as compared with TMB + Cat and TMB +  $H_2O_2$ , as the former needed a much longer time to reach a steady state than the latter two [68]. One of the crucial factors in a catalytic reaction is the temperature. In this study, the dependence of the catalytic activity of  $Fe_3C/N-C$  on the reaction temperature was studied in the range from 25 to 60 °C. Figure 3c and Figure S11 demonstrate that the optimum reaction temperature for our peroxidase catalyst is 40 °C, which is close to the human body temperature, so it is more applicable for vitamin C detection in the biological samples, e.g., human serums. Regarding the drop in activity over 40 °C, similar phenomena have been illustrated by Biswas et al. [69]. Furthermore, the effect of pH on catalytic activity was investigated in the range of 2.0–11.0 (Figure 3d and Figure S12). In strong acidic media (at pH of 2.0), a pale blue color was obtained. At pH 3.0 and pH 5.0, the system revealed a slight blue color with 50% relative activity. A solid blue

color was detected at pH 4.0, suggesting the best catalytic activity of the sample at pH ~4.0. According to previous studies, HRP also showed similar behavior [64]. Thus, the pH value for the further catalytic studies was chosen to be 4.0. The UV-Vis absorbance spectrum of TMB oxidation was assessed by changing the concentrations of TMB (0.02–1 mM) and H<sub>2</sub>O<sub>2</sub> (7–80 mM). The tests showed that optimum absorbance occurred at 0.2 mM TMB (Figure S13) and 50 mM H<sub>2</sub>O<sub>2</sub> (Figure S14). Furthermore, the performance of the catalyst in both membrane and powder states was compared with each other (Figure 3e), which illustrated that the catalytic activity of powder and membrane catalysts was practically the same. This observation proves that the membrane shape due of its low thickness did not retard the reaction kinetics, thanks to the hierarchical porous structure and high surface. In addition, the activity of the nitrogen-free pure carbon membrane, obtained from the carbonization of pure Balsa wood under the same condition, was measured as a control test; the result asserts that the presence of Fe<sub>3</sub>C nanoparticles and nitrogen doping is essential in this application. Due to the free-standing membrane shape of the Fe<sub>3</sub>C/N-C, it is easy to recycle it, thus reducing the cost by simple recycling. In Figure 3f, it is observed that the activity of our hierarchical porous membrane catalyst remains at 90% of the initial activity after 10 cycles, demonstrating its astonishing robustness in repeated use.

The steady-state kinetic factors for the mimetic peroxidase reaction were determined by altering the concentration of one substrate while keeping the others constant. The catalytic performance of the Fe<sub>3</sub>C/N-C was profoundly probed through the kinetic analysis employing the TMB and H<sub>2</sub>O<sub>2</sub> concentration as the variable. Figure 4a,c reveal the typical Michaelis–Menten curves; from the achieved curves, their Lineweaver–Burk plots were gained, as shown in Figure 4b,d. The initial velocity of ox-TMB was analyzed from the absorbance data, and the molar attenuation coefficient of TMB at 652 nm was 39,000 M<sup>-1</sup>cm<sup>-1</sup> by using the Lambert–Beer (Equation (2)) law as shown below.

$$A = \epsilon cb \quad (2)$$

where  $A$ ,  $\epsilon$ ,  $c$ , and  $b$  are denoted as the absorbance, molar absorbance coefficient, substrate concentration, and the thickness of the sample, respectively. The Michaelis–Menten constant ( $K_m$ ) and maximum velocity ( $V_{max}$ ) were obtained from Equation (3).

$$\frac{1}{V} = \frac{K_m}{V_{max}} \cdot \frac{1}{[S]} + \frac{1}{V_{max}} \quad (3)$$

where  $V$  represents the initial reaction rate,  $V_{max}$  represents the maximum initial rate,  $K_m$  represents the Michaelis–Menten constant, and  $[S]$  represents the substrate concentration. It is known that the catalytic power of a sample depends on the  $K_m$  and  $V_{max}$  values [70,71]. The  $K_m$  value indicates attraction among the enzyme and substrate, with a lower  $K_m$  value representing a stronger affinity between the enzyme and substrate. The larger  $V_{max}$  value proposes a better efficiency for TMB oxidation in the presence of hydrogen peroxide. In this study, the  $K_m$  and  $V_{max}$  values of the Fe<sub>3</sub>C/N-C catalyst for TMB were calculated to be 0.033 mM and  $4.2 \times 10^{-8}$  Ms<sup>-1</sup>, respectively. The  $K_m$  value was about 15 times smaller than that of HRP (0.41 mM) [39], suggesting an improved affinity of the catalyst to TMB than that of HRP. This effect could stem from the high surface area, the hierarchical porous structure, and the presence of ultrafine Fe<sub>3</sub>C nanoparticles in Fe<sub>3</sub>C/N-C, which developed more active sites for TMB and a lower  $K_m$  value [3]. The  $K_m$  and  $V_{max}$  values were compared with HRP and several other nanomaterials, as shown in Table S1. It is worth mentioning that less than 5 min was required to see the distinguishable color difference in the Fe<sub>3</sub>C/N-C system. These results suggest that Fe<sub>3</sub>C/N-C is efficient and needs a shorter time for colorimetric study than other similar mimetic peroxidases (usually more than 10 min). Such properties are vital factors for a rapid visual colorimetric test.

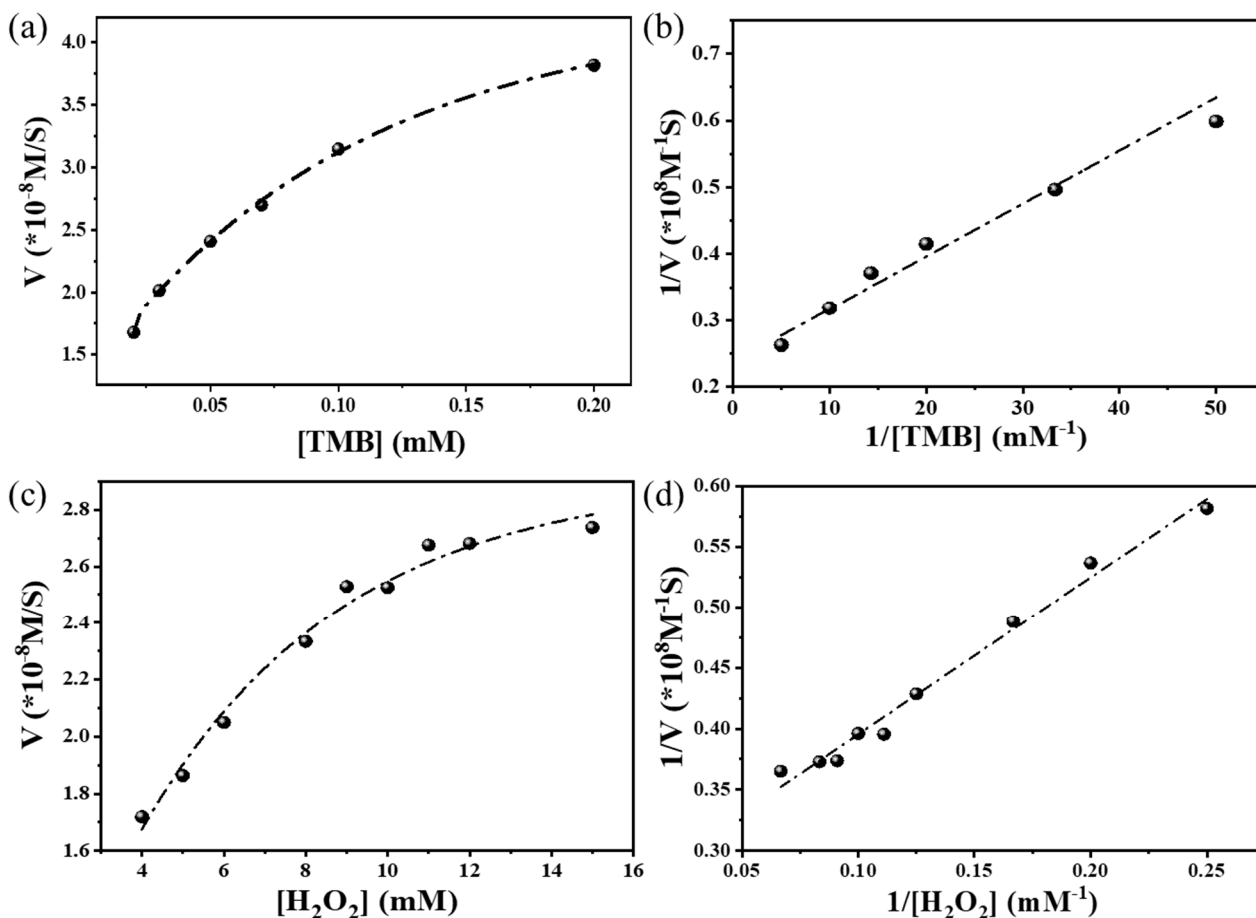


**Figure 4.** Steady-state kinetic experiments of Fe<sub>3</sub>C/N-C for catalytic tests. (a) The concentration of H<sub>2</sub>O<sub>2</sub> was 50 mM and the TMB concentration varied. (b) Lineweaver–Burk plots for TMB substrate. (c) The concentration of TMB was 200  $\mu\text{M}$  and the H<sub>2</sub>O<sub>2</sub> concentration varied. (d) Lineweaver–Burk plots for H<sub>2</sub>O<sub>2</sub> substrate. An amount of 20  $\mu\text{L}$  of catalyst (3  $\text{mg}\cdot\text{L}^{-1}$ ) was used in this experiment conducted at room temperature.

**Colorimetric detection of ascorbic acid using the peroxidase-like catalytic reaction of Fe<sub>3</sub>C/N-C.** Because of the intrinsic peroxidase property of the Fe<sub>3</sub>C/N-C, we designed a colorimetric system to detect AA in aqueous solutions, using the same substrate studied above, i.e., TMB and H<sub>2</sub>O<sub>2</sub>. The detection of vitamin C is according to its antioxidant nature of preventing oxidation via reducing the reactive free radicals [72,73]. Hence, the corresponding UV-Vis absorbance spectrum of the Fe<sub>3</sub>C/N-C-TMB-H<sub>2</sub>O<sub>2</sub> system versus vitamin C concentration ([AA]) from 0 to 200  $\mu\text{M}$  is presented in Figure 5a, and the linear relationship between  $\Delta A$  (the difference between UV-Vis absorbance before and after adding AA) and [AA] was gained in the range of 2–50  $\mu\text{M}$  ( $R^2$ : 0.993) (Figure 5b). The limit of detection was around 2.64  $\mu\text{M}$ , which is better than many other reports (Table S2).

To evaluate the selectivity of detection of AA by monitoring the absorbance of the reaction systems, vitamin C was replaced by various biologically relevant species such as sulfite, citric acid, glycine, serine, alanine, aspartic acid, tartaric acid, arginine, and saccharides like glucose, lactose, and fructose. The significant change in the absorbance intensity at 652 nm was not noticed after adding other interferences. Figure 5c depicts the  $\Delta A$  values of those systems. The considerable difference in the  $\Delta A$  values among the mentioned interferences and vitamin C at similar concentrations can be clearly seen. These outcomes prove the outstanding specificity of our sensing process to the colorimetric detection of AA.

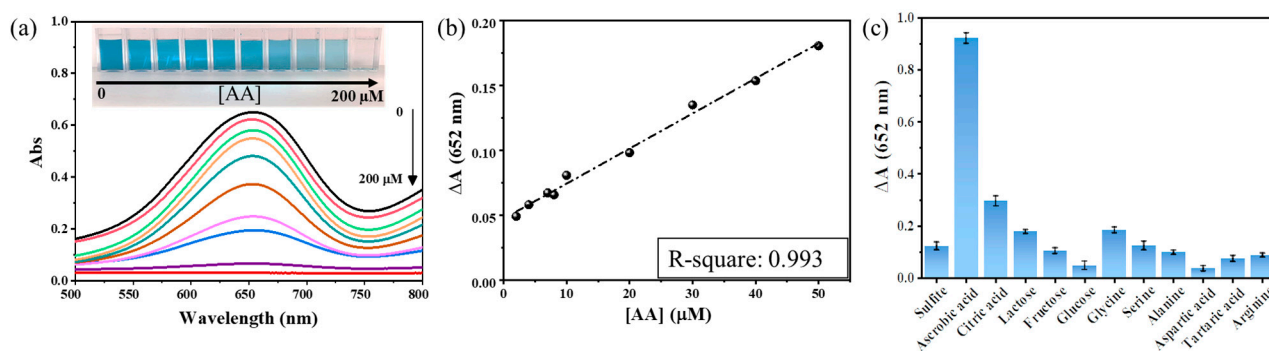


**Figure 5.** (a) Absorbance changes of the mixing solution consisting of TMB, the catalyst suspension, and  $H_2O_2$  in the absence or presence of ascorbic acid and corresponding optical photographs. (b) Linear calibration plot to detect ascorbic acid.  $\Delta A = A(652 \text{ nm, absence}) - A(652 \text{ nm, ascorbic acid})$ . (c)  $\Delta A$  values of the  $Fe_3C/N-C-TMB-H_2O_2$  system at 652 nm in the presence of ascorbic acid or other interferential substances.

#### 4. Conclusions

In summary, uniformly dispersed  $Fe_3C$  nanoparticles were introduced into a hierarchically porous nitrogen-doped carbon membrane derived from a thin wood slice pre-coated by PIL and  $FeCl_3$  before carbonization. Owing to the unique interconnected and oriented porous structure, ultrafine nanoparticles, and nitrogen doping, the as-prepared  $Fe_3C/N-C$  catalyst demonstrated outstanding intrinsic peroxidase-like catalytic activity with favorable stability and recyclability, which could be utilized to sensitively detect ascorbic acid over a broad concentration range with a low limit of detection ( $\sim 2.64 \mu M$ ). The detection system exhibited a high selectivity and anti-interference capacity to ascorbic acid. This study proposes a straightforward and effective way for preparing metal-containing heteroatom-doped porous carbon membranes, which can be generalized to synthesize various other functional carbonaceous materials such as artificial enzymes, revealing great potential in medicine, biosensing, and environmental fields.

**Supplementary Materials:** The following supporting information can be downloaded at <https://www.mdpi.com/article/10.3390/nano13202786/s1>. Additional results such as Figure S1:  $^1H-NMR$  of the PIL, Figure S2: UV–Vis absorbance spectra of the ox-TMB, Figure S3: Cross-sectional SEM images of  $Fe_3C/N-C$ , Figure S4: Nanoparticle size distribution of  $Fe_3C/N-C$  based on the TEM image, Figure S5: TEM image of  $Fe_3C/N-C$  when PIL wasn't used to disperse iron source, Figure S6: Particle size distribution of  $Fe_3C/N-C$  when PIL wasn't used to disperse iron source, Figure S7: TGA curve of  $Fe_3C/N-C$  under air, Figure S8: PXRD diagram of the TGA residue of  $\nu$ , Figure S9: Nitrogen sorption isotherm of  $Fe_3C/N-C$ , Figure S10: Pore size distribution plot of  $Fe_3C/N-C$ , Figure S11: Temperature dependence plot of the peroxidase-like activity, Figure S12: pH dependence of the peroxidase-like activity, Figure S13: TMB concentration dependence of the peroxidase-like activity, Figure S14:  $H_2O_2$  concentration dependence of the peroxidase-like activity, Table S1: Comparison of the apparent Michaelis constant ( $K_m$ ) and maximum reaction rate ( $V_{max}$ ) between our work and other groups' work, Table S2: Analytical characteristics of different colorimetric AA measuring system. References [74–82] are cited in the supplementary materials.

**Author Contributions:** S.S.G., K.P. and D.X. co-conducted all experiments. S.S.G. and A.S. wrote the manuscript draft. M.Z. and J.Y. defined the project concept, supervised the synthesis of materials and the colorimetric tests, and corrected the manuscript. All authors have read and agreed to the published version of the manuscript.

**Funding:** J.Y. is grateful for financial support from the Swedish Research Council Grant 2018-05351, and the Wallenberg Academy Fellow program from the Knut and Alice Wallenberg Foundation (Grant KAW 2017.0166) in Sweden.

**Data Availability Statement:** Data will be available upon request.

**Acknowledgments:** The authors thank Atefeh Khorsand Kheirabad at Stockholm University for helping synthesize PILs and Ehsan Hadi at Stockholm University for capturing TEM images in the supporting information.

**Conflicts of Interest:** The authors declare no conflict of interest.

## References

1. Du, J.; Cullen, J.J.; Buettner, G.R. Ascorbic Acid: Chemistry, Biology and the Treatment of Cancer. *Biochim. Biophys. Acta Rev. Cancer* **2012**, *1826*, 443–457. [[CrossRef](#)] [[PubMed](#)]
2. van Robertson, W.B.; Schwartz, B. Ascorbic Acid and the Formation of Collagen. *J. Biol. Chem.* **1953**, *201*, 689–696. [[CrossRef](#)] [[PubMed](#)]
3. Zheng, X.; Lian, Q.; Zhou, L.; Jiang, Y.; Gao, J. Peroxidase Mimicking of Binary Polyacrylonitrile-CuO Nanoflowers and the Application in Colorimetric Detection of H<sub>2</sub>O<sub>2</sub> and Ascorbic Acid. *ACS Sustain. Chem. Eng.* **2021**, *9*, 7030–7043. [[CrossRef](#)]
4. Szultka, M.; Buszewska-Forajta, M.; Kaliszczan, R.; Buszewski, B. Determination of Ascorbic Acid and Its Degradation Products by High-Performance Liquid Chromatography-Triple Quadrupole Mass Spectrometry. *Electrophoresis* **2014**, *35*, 585–592. [[CrossRef](#)] [[PubMed](#)]
5. He, P.; Niu, Y.; Mei, Z.; Bao, J.; Sun, X. Measurement of Ascorbic Acid in Single Rat Peritoneal Mast Cells Using Capillary Electrophoresis with Electrochemical Detection. *J. Chromatogr. B Anal. Technol. Biomed. Life Sci.* **2010**, *878*, 1093–1097. [[CrossRef](#)] [[PubMed](#)]
6. Malashikhina, N.; Pavlov, V. DNA-Decorated Nanoparticles as Nanosensors for Rapid Detection of Ascorbic Acid. *Biosens. Bioelectron.* **2012**, *33*, 241–246. [[CrossRef](#)]
7. Cheng, H.; Wang, X.; Wei, H. Ratiometric Electrochemical Sensor for Effective and Reliable Detection of Ascorbic Acid in Living Brains. *Anal. Chem.* **2015**, *87*, 8889–8895. [[CrossRef](#)] [[PubMed](#)]
8. Keerthana, S.; Rajapriya, A.; Viswanathan, C.; Ponpandian, N. Enzyme Like-Colorimetric Sensing of H<sub>2</sub>O<sub>2</sub> Based on Intrinsic Peroxidase Mimic Activity of WS<sub>2</sub> Nanosheets Anchored Reduced Graphene Oxide. *J. Alloys Compd.* **2022**, *889*, 161669. [[CrossRef](#)]
9. Wei, H.; Wang, E. Nanomaterials with Enzyme-like Characteristics (Nanozymes): Next-Generation Artificial Enzymes. *Chem. Soc. Rev.* **2013**, *42*, 6060–6093. [[CrossRef](#)]
10. Wu, J.; Wang, X.; Wang, Q.; Lou, Z.; Li, S.; Zhu, Y.; Qin, L.; Wei, H. Nanomaterials with Enzyme-like Characteristics (Nanozymes): Next-Generation Artificial Enzymes (II). *Chem. Soc. Rev.* **2019**, *48*, 1004–1076. [[CrossRef](#)]
11. Xing, Z.; Tian, J.; Asiri, A.M.; Qusti, A.H.; Al-Youbi, A.O.; Sun, X. Two-Dimensional Hybrid Mesoporous Fe<sub>2</sub>O<sub>3</sub>-Graphene Nanostructures: A Highly Active and Reusable Peroxidase Mimetic toward Rapid, Highly Sensitive Optical Detection of Glucose. *Biosens. Bioelectron.* **2014**, *52*, 452–457. [[CrossRef](#)] [[PubMed](#)]
12. Biswas, S.; Tripathi, P.; Kumar, N.; Nara, S. Gold Nanorods as Peroxidase Mimetics and Its Application for Colorimetric Biosensing of Malathion. *Sens. Actuators B Chem.* **2016**, *231*, 584–592. [[CrossRef](#)]
13. Masud, M.K.; Na, J.; Younus, M.; Hossain, M.S.A.; Bando, Y.; Shiddiky, M.J.A.; Yamauchi, Y. Superparamagnetic Nanoarchitectures for Disease-Specific Biomarker Detection. *Chem. Soc. Rev.* **2019**, *48*, 5717–5751. [[CrossRef](#)] [[PubMed](#)]
14. Zhang, P.; Sun, D.; Cho, A.; Weon, S.; Lee, S.; Lee, J.; Han, J.W.; Kim, D.P.; Choi, W. Modified Carbon Nitride Nanozyme as Bifunctional Glucose Oxidase-Peroxidase for Metal-Free Bioinspired Cascade Photocatalysis. *Nat. Commun.* **2019**, *10*, 940. [[CrossRef](#)] [[PubMed](#)]
15. Garg, B.; Bisht, T.; Ling, Y.C. Graphene-Based Nanomaterials as Efficient Peroxidase Mimetic Catalysts for Biosensing Applications: An Overview. *Molecules* **2015**, *20*, 14155–14190. [[CrossRef](#)] [[PubMed](#)]
16. Guo, L.; Liu, Y.; Kong, R.; Chen, G.; Liu, Z.; Qu, F.; Xia, L.; Tan, W. A Metal-Organic Framework as Selectivity Regulator for Fe<sup>3+</sup> and Ascorbic Acid Detection. *Anal. Chem.* **2019**, *91*, 12453–12460. [[CrossRef](#)]
17. Zhao, Y.; Zhang, J.; Guo, X.; Fan, H.; Wu, W.; Liu, H.; Wang, G. Fe<sub>3</sub>C@nitrogen Doped CNT Arrays Aligned on Nitrogen Functionalized Carbon Nanofibers as Highly Efficient Catalysts for the Oxygen Evolution Reaction. *J. Mater. Chem. A* **2017**, *5*, 19672–19679. [[CrossRef](#)]
18. Song, N.; Ma, F.; Zhu, Y.; Chen, S.; Wang, C.; Lu, X. Fe<sub>3</sub>C/Nitrogen-Doped Carbon Nanofibers as Highly Efficient Biocatalyst with Oxidase-Mimicking Activity for Colorimetric Sensing. *ACS Sustain. Chem. Eng.* **2018**, *6*, 16766–16776. [[CrossRef](#)]
19. Hu, M.; Lin, Y.; Li, X.; Zhang, W.; Chen, Z.; Yang, Y.; Li, G.; Lu, Y.; Li, W. Nano-Fe<sub>3</sub>C@2D-NC@CC as Anode for Improving Extracellular Electron Transfer and Electricity Generation of Microbial Fuel Cells. *Electrochim. Acta* **2022**, *404*, 139618. [[CrossRef](#)]
20. Fletcher, D.C.; Hunter, R.; Xia, W.; Smales, G.J.; Pauw, B.R.; Blackburn, E.; Kulak, A.; Xin, H.; Schnepf, Z. Scalable Synthesis of Dispersible Iron Carbide (Fe<sub>3</sub>C) Nanoparticles by “Nanocasting”. *J. Mater. Chem. A* **2019**, *7*, 19506–19512. [[CrossRef](#)]
21. Xi, X.; Peng, X.; Xiong, C.; Shi, D.; Zhu, J.; Wen, W.; Zhang, X.; Wang, S. Iron Doped Graphitic Carbon Nitride with Peroxidase like Activity for Colorimetric Detection of Sarcosine and Hydrogen Peroxide. *Microchim. Acta* **2020**, *187*, 383. [[CrossRef](#)] [[PubMed](#)]
22. Wang, X.; Hu, Z.; Li, Z.; Jiao, L.; Hou, L.; Ma, F.; He, Y.; Feng, X. Fe<sub>3</sub>C Encapsulated in N-Doped Carbon Shell Grown on Reduced Graphene Oxide as a High-Performance Negative Material for Electrochemical Energy Storage. *Chem. Eng. J.* **2021**, *412*, 128720. [[CrossRef](#)]
23. Qu, K.; Zheng, Y.; Jiao, Y.; Zhang, X.; Dai, S.; Qiao, S.Z. Polydopamine-Inspired, Dual Heteroatom-Doped Carbon Nanotubes for Highly Efficient Overall Water Splitting. *Adv. Energy Mater.* **2017**, *7*, 1602068. [[CrossRef](#)]

24. Yuan, J.; Giordano, C.; Antonietti, M. Ionic Liquid Monomers and Polymers as Precursors of Highly Conductive, Mesoporous, Graphitic Carbon Nanostructures. *Chem. Mater.* **2010**, *22*, 5003–5012. [[CrossRef](#)]
25. Hunter, R.D.; Rowlandson, J.L.; Smales, G.J.; Pauw, B.R.; Ting, V.P.; Kulak, A.; Schnepf, Z. The Effect of Precursor Structure on Porous Carbons Produced by Iron-Catalyzed Graphitization of Biomass. *Mater. Adv.* **2020**, *1*, 3281–3291. [[CrossRef](#)]
26. Yuan, J.; Universitet, S.; Zhang, M.; Zhang, M.; Wang, W.; Eriksson, M.; Wu, M.; Wang, H.; Qu, L.; Yuan, J.; et al. From Wood to Thin Porous Carbon Membrane: Ancient Materials for Modern Ultrafast Electrochemical Capacitors in Alternating Current Line Filtering. *Energy Storage Mater.* **2021**, *35*, 327–333.
27. Wu, Y.; Zhang, N.; de Lannoy, C.F. Fast Synthesis of High Surface Area Bio-Based Porous Carbons for Organic Pollutant Removal. *MethodsX* **2021**, *8*, 101464. [[CrossRef](#)]
28. Men, Y.; Siebenbürger, M.; Qiu, X.; Antonietti, M.; Yuan, J. Low Fractions of Ionic Liquid or Poly(Ionic Liquid) Can Activate Polysaccharide Biomass into Shaped, Flexible and Fire-Retardant Porous Carbons. *J. Mater. Chem. A* **2013**, *1*, 11887–11893. [[CrossRef](#)]
29. Miao, L.; Duan, H.; Wang, Z.; Lv, Y.; Xiong, W.; Zhu, D.; Gan, L.; Li, L.; Liu, M. Improving the Pore-Ion Size Compatibility between Poly(Ionic Liquid)-Derived Carbons and High-Voltage Electrolytes for High Energy-Power Supercapacitors. *Chem. Eng. J.* **2020**, *382*, 122945. [[CrossRef](#)]
30. Li, H.; Zhang, C.; Yan, Y.; Hu, K.; Shi, X.; Wang, N.; Lin, H.; Rui, K.; Zhu, J.; Huang, W. Poly(Ionic Liquid) Derived N-Doped Carbon@SnO<sub>x</sub> Nanostructures Self-Reconstruction for Alkaline-Metal-Ion Batteries. *J. Power Sources* **2020**, *449*, 227509. [[CrossRef](#)]
31. Zhang, M.; Dong, K.; Saeedi Garakani, S.; Khorsand Kheirabad, A.; Manke, I.; Wu, M.; Wang, H.; Qu, L.; Yuan, J. Bridged Carbon Fabric Membrane with Boosted Performance in AC Line-Filtering Capacitors. *Adv. Sci.* **2022**, *9*, 2105072. [[CrossRef](#)]
32. Lin, H.; Zhang, S.; Sun, J.K.; Antonietti, M.; Yuan, J. Poly(Ionic Liquid)s with Engineered Nanopores for Energy and Environmental Applications. *Polymer* **2020**, *202*, 122640. [[CrossRef](#)]
33. Khorsand Kheirabad, A.; Saeedi Garakani, S.; Tan, L.; Yuan, J. Ferrocene-Containing Porous Poly(Ionic Liquid) Membranes: Synthesis and Application as Sacrificial Template for Porous Iron Oxide Films. *Macromol. Rapid Commun.* **2021**, *42*, 2100077. [[CrossRef](#)] [[PubMed](#)]
34. Zhao, X.; Zhang, Z.; Song, N.; Shi, J.; Yang, N.; Nie, G.; Wang, C. Vanadium/Cobalt Oxides-Anchored Flexible Carbon Nanofibers with Tunable Magnetism as Recoverable Peroxidase-like Catalysts. *Mater. Today Chem.* **2021**, *22*, 100568. [[CrossRef](#)]
35. Zhang, K.; Lu, L.; Liu, Z.; Cao, X.; Lv, L.; Xia, J.; Wang, Z. Colloids and Surfaces A: Physicochemical and Engineering Aspects Metal-Organic Frameworks-Derived Bimetallic Oxide Composite Nanozyme Fiber Membrane and the Application to Colorimetric Detection of Phenol. *Colloids Surfaces A Physicochem. Eng. Asp.* **2022**, *650*, 129662. [[CrossRef](#)]
36. Wang, Y.C.; Wan, L.Y.; Cui, P.X.; Tong, L.; Ke, Y.Q.; Sheng, T.; Zhang, M.; Sun, S.H.; Liang, H.W.; Wang, Y.S.; et al. Porous Carbon Membrane-Supported Atomically Dispersed Pyrrole-Type Fe-N<sub>4</sub> as Active Sites for Electrochemical Hydrazine Oxidation Reaction. *Small* **2020**, *16*, 2002203. [[CrossRef](#)] [[PubMed](#)]
37. Adam, M.; Oschatz, M.; Nickel, W.; Kaskel, S. Preparation of Hierarchical Porous Biomorphic Carbide-Derived Carbon by Polycarbosilane Impregnation of Wood. *Microporous Mesoporous Mater.* **2015**, *210*, 26–31. [[CrossRef](#)]
38. Song, H.; Xu, S.; Li, Y.; Dai, J.; Gong, A.; Zhu, M.; Zhu, C.; Chen, C.; Chen, Y.; Yao, Y.; et al. Hierarchically Porous, Ultrathick, “Breathable” Wood-Derived Cathode for Lithium-Oxygen Batteries. *Adv. Energy Mater.* **2018**, *8*, 1701203. [[CrossRef](#)]
39. Wu, S.; Huang, H.; Feng, X.; Du, C.; Song, W. Facile Visual Colorimetric Sensor Based on Iron Carbide Nanoparticles Encapsulated in Porous Nitrogen-Rich Graphene. *Talanta* **2017**, *167*, 385–391. [[CrossRef](#)]
40. Saeedi Garakani, S.; Xie, D.; Kheirabad, A.K.; Lu, Y.; Yuan, J. Template-Synthesis of a Poly(Ionic Liquid)-Derived Fe<sub>1-x</sub>S/Nitrogen-Doped Porous Carbon Membrane and Its Electrode Application in Lithium-Sulfur Batteries. *Mater. Adv.* **2021**, *2*, 5203–5212. [[CrossRef](#)]
41. Jiang, W.J.; Gu, L.; Li, L.; Zhang, Y.; Zhang, X.; Zhang, L.J.; Wang, J.Q.; Hu, J.S.; Wei, Z.; Wan, L.J. Understanding the High Activity of Fe-N-C Electrocatalysts in Oxygen Reduction: Fe/Fe<sub>3</sub>C Nanoparticles Boost the Activity of Fe-N<sub>x</sub>. *J. Am. Chem. Soc.* **2016**, *138*, 3570–3578. [[CrossRef](#)] [[PubMed](#)]
42. Cai, B.; Feng, J.; Peng, Q.; Zhao, H.; Miao, Y.; Pan, H. Super-Fast Degradation of High Concentration Methyl Orange over Bifunctional Catalyst Fe/Fe<sub>3</sub>C@C with Microwave Irradiation. *J. Hazard. Mater.* **2020**, *392*, 122279. [[CrossRef](#)]
43. Wu, Y.; Zhang, N.; Yuen, G.; de Lannoy, C.F. Cross-Linked Iron Nanoparticle-Doped Reduced Graphene Oxide Membranes for Micropollutant Removal from Water. *Chem. Eng. J.* **2022**, *455*, 140624. [[CrossRef](#)]
44. Sun, Y.; Wang, Y.; Ma, H.; Zhou, Y.; Xing, H.; Feng, W.; Feng, J.; Shi, Z.; Zong, Y.; Li, X.; et al. Fe<sub>3</sub>C Nanocrystals Encapsulated in N-Doped Carbon Nanofibers as High-Efficient Microwave Absorbers with Superior Oxidation/Corrosion Resistance. *Carbon* **2021**, *178*, 515–527. [[CrossRef](#)]
45. Jiang, H.; Yao, Y.; Zhu, Y.; Liu, Y.; Su, Y.; Yang, X.; Li, C. Iron Carbide Nanoparticles Encapsulated in Mesoporous Fe-N-Doped Graphene-Like Carbon Hybrids as Efficient Bifunctional Oxygen Electrocatalysts. *ACS Appl. Mater. Interfaces* **2015**, *7*, 21511–21520. [[CrossRef](#)] [[PubMed](#)]
46. Jeon, I.Y.; Zhang, S.; Zhang, L.; Choi, H.J.; Seo, J.M.; Xia, Z.; Dai, L.; Baek, J.B. Edge-Selectively Sulfurized Graphene Nanoplatelets as Efficient Metal-Free Electrocatalysts for Oxygen Reduction Reaction: The Electron Spin Effect. *Adv. Mater.* **2013**, *25*, 6138–6145. [[CrossRef](#)] [[PubMed](#)]
47. Zou, M.; Wang, L.; Li, J.; Guan, L.; Huang, Z. Enhanced Li-Ion Battery Performances of Yolk-Shell Fe<sub>3</sub>O<sub>4</sub>@C Anodes with Fe<sub>3</sub>C Catalyst. *Electrochim. Acta* **2017**, *233*, 85–91. [[CrossRef](#)]

48. Dai, J.; Tian, S.; Jiang, Y.; Chang, Z.; Xie, A.; Zhang, R.; Li, C.; Yan, Y. Fe<sub>3</sub>C/Fe/C Magnetic Hierarchical Porous Carbon with Micromesopores for Highly Efficient Chloramphenicol Adsorption: Magnetization, Graphitization, and Adsorption Properties Investigation. *Ind. Eng. Chem. Res.* **2018**, *57*, 3510–3522. [[CrossRef](#)]
49. Zhao, K.; Nie, X.; Wang, H.; Chen, S.; Quan, X.; Yu, H.; Choi, W.; Zhang, G.; Kim, B.; Chen, J.G. Selective Electroreduction of CO<sub>2</sub> to Acetone by Single Copper Atoms Anchored on N-Doped Porous Carbon. *Nat. Commun.* **2020**, *11*, 2455. [[CrossRef](#)]
50. Qu, K.; Zheng, Y.; Zhang, X.; Davey, K.; Dai, S.; Qiao, S.Z. Promotion of Electrocatalytic Hydrogen Evolution Reaction on Nitrogen-Doped Carbon Nanosheets with Secondary Heteroatoms. *ACS Nano* **2017**, *11*, 7293–7300. [[CrossRef](#)]
51. Ma, W.; Du, Y.; Wang, N.; Miao, P. ZIF-8 Derived Nitrogen-Doped Porous Carbon as Metal-Free Catalyst of Peroxymonosulfate Activation. *Environ. Sci. Pollut. Res.* **2017**, *24*, 16276–16288. [[CrossRef](#)]
52. Ma, W.; Wang, N.; Du, Y.; Tong, T.; Zhang, L.; Andrew Lin, K.Y.; Han, X. One-Step Synthesis of Novel Fe<sub>3</sub>C@nitrogen-Doped Carbon Nanotubes/Graphene Nanosheets for Catalytic Degradation of Bisphenol A in the Presence of Peroxymonosulfate. *Chem. Eng. J.* **2019**, *356*, 1022–1031. [[CrossRef](#)]
53. Guo, C.; Chen, C.; Lu, J.; Fu, D.; Yuan, C.Z.; Wu, X.L.; Hui, K.N.; Chen, J. Stable and Recyclable Fe<sub>3</sub>C@CN Catalyst Supported on Carbon Felt for Efficient Activation of Peroxymonosulfate. *J. Colloid Interface Sci.* **2021**, *599*, 219–226. [[CrossRef](#)] [[PubMed](#)]
54. Joshi, B.; Lee, J.G.; Samuel, E.; Jo, H.S.; Kim, T.G.; Swihart, M.T.; Yoon, W.Y.; Yoon, S.S. Supersonically Blown Reduced Graphene Oxide Loaded Fe-Fe<sub>3</sub>C Nanofibers for Lithium Ion Battery Anodes. *J. Alloys Compd.* **2017**, *726*, 114–120. [[CrossRef](#)]
55. Lin, G.; Ma, R.; Zhou, Y.; Hu, C.; Yang, M.; Liu, Q.; Kaskel, S.; Wang, J. Three-Dimensional Interconnected Nitrogen-Doped Mesoporous Carbons as Active Electrode Materials for Application in Electrocatalytic Oxygen Reduction and Supercapacitors. *J. Colloid Interface Sci.* **2018**, *527*, 230–240. [[CrossRef](#)] [[PubMed](#)]
56. Zhang, Y.; Jiao, L.; Xu, W.; Chen, Y.; Wu, Y.; Yan, H.; Gu, W.; Zhu, C. Defect-Rich and Ultrathin Nitrogen-Doped Carbon Nanosheets with Enhanced Peroxidase-like Activity for the Detection of Urease Activity and Fluoride Ion. *Chin. Chem. Lett.* **2022**, *33*, 1317–1320. [[CrossRef](#)]
57. Miao, L.; Duan, H.; Liu, M.; Lu, W.; Zhu, D.; Chen, T.; Li, L.; Gan, L. Poly(Ionic Liquid)-Derived, N, S-Codoped Ultramicroporous Carbon Nanoparticles for Supercapacitors. *Chem. Eng. J.* **2017**, *317*, 651–659. [[CrossRef](#)]
58. Chen, Y.; Jiao, L.; Yan, H.; Xu, W.; Wu, Y.; Wang, H.; Gu, W.; Zhu, C. Hierarchically Porous S/N Codoped Carbon Nanozymes with Enhanced Peroxidase-like Activity for Total Antioxidant Capacity Biosensing. *Anal. Chem.* **2020**, *92*, 13518–13524. [[CrossRef](#)] [[PubMed](#)]
59. Wang, S.; Wang, M.; Liu, Y.; Meng, X.; Ye, Y.; Song, X.; Liang, Z. Novel D- $\pi$ -A Conjugated Microporous Polymer as Visible Light-Driven Oxidase Mimic for Efficient Colorimetric Detection of Glutathione. *Sens. Actuators B Chem.* **2021**, *326*, 128808. [[CrossRef](#)]
60. Chen, Q.; Li, S.; Liu, Y.; Zhang, X.; Tang, Y.; Chai, H.; Huang, Y. Size-Controllable Fe-N/C Single-Atom Nanozyme with Exceptional Oxidase-like Activity for Sensitive Detection of Alkaline Phosphatase. *Sens. Actuators B Chem.* **2020**, *305*, 127511. [[CrossRef](#)]
61. Yang, X.; Wang, Y.; Zhang, G.; Du, L.; Yang, L.; Markiewicz, M.; Choi, J.; Chenitz, R.; Sun, S. SiO<sub>2</sub>-Fe/N/C Catalyst with Enhanced Mass Transport in PEM Fuel Cells. *Appl. Catal. B Environ.* **2020**, *264*, 118523. [[CrossRef](#)]
62. Yang, H.; Xiao, J.; Su, L.; Feng, T.; Lv, Q.; Zhang, X. Oxidase-Mimicking Activity of the Nitrogen-Doped Fe<sub>3</sub>C@C Composites. *Chem. Commun.* **2017**, *53*, 3882–3885. [[CrossRef](#)] [[PubMed](#)]
63. Lin, Y.; Ren, J.; Qu, X. Catalytically Active Nanomaterials: A Promising Candidate for Artificial Enzymes. *Acc. Chem. Res.* **2014**, *47*, 1097–1105. [[CrossRef](#)] [[PubMed](#)]
64. Gao, L.; Zhuang, J.; Nie, L.; Zhang, J.; Zhang, Y.; Gu, N.; Wang, T.; Feng, J.; Yang, D.; Perrett, S.; et al. Intrinsic Peroxidase-like Activity of Ferromagnetic Nanoparticles. *Nat. Nanotechnol.* **2007**, *2*, 577–583. [[CrossRef](#)] [[PubMed](#)]
65. Masud, M.K.; Yadav, S.; Islam, M.N.; Nguyen, N.T.; Salomon, C.; Kline, R.; Alamri, H.R.; Alothman, Z.A.; Yamauchi, Y.; Hossain, M.S.A.; et al. Gold-Loaded Nanoporous Ferric Oxide Nanocubes with Peroxidase-Mimicking Activity for Electrocatalytic and Colorimetric Detection of Autoantibody. *Anal. Chem.* **2017**, *89*, 11005–11013. [[CrossRef](#)] [[PubMed](#)]
66. Li, Y.; Ma, W.; Sun, J.; Lin, M.; Niu, Y.; Yang, X.; Xu, Y. Electrochemical Generation of Fe<sub>3</sub>C/N-Doped Graphitic Carbon Nanozyme for Efficient Wound Healing in Vivo. *Carbon* **2020**, *159*, 149–160. [[CrossRef](#)]
67. Lv, N.; Wang, T.; Zhao, Z.; Mu, S.; Zhu, H.; Bai, M.; Gao, Y.; Ma, L.; Luo, X.; Cheng, C. Creating Efficient and Specific Peroxidase-Like Atomic Cu-N-C Centers via Axial Strong-Metal-Support-Interaction for Enzymatic Biodetection. *Adv. Mater. Technol.* **2023**, *8*, 2300130. [[CrossRef](#)]
68. Zhu, J.; Nie, W.; Wang, Q.; Li, J.; Li, H.; Wen, W.; Bao, T.; Xiong, H.; Zhang, X.; Wang, S. In Situ Growth of Copper Oxide-Graphite Carbon Nitride Nanocomposites with Peroxidase-Mimicking Activity for Electrocatalytic and Colorimetric Detection of Hydrogen Peroxide. *Carbon* **2018**, *129*, 29–37. [[CrossRef](#)]
69. Dutta, A.K.; Das, S.; Samanta, S.; Samanta, P.K.; Adhikary, B.; Biswas, P. CuS Nanoparticles as a Mimic Peroxidase for Colorimetric Estimation of Human Blood Glucose Level. *Talanta* **2013**, *107*, 361–367. [[CrossRef](#)]
70. Masud, M.K.; Kim, J.; Billah, M.M.; Wood, K.; Shiddiky, M.J.A.; Nguyen, N.T.; Parsapur, R.K.; Kaneti, Y.V.; Alshehri, A.A.; Alghamidi, Y.G.; et al. Nanoarchitected Peroxidase-Mimetic Nanozymes: Mesoporous Nanocrystalline  $\alpha$ - or  $\gamma$ -Iron Oxide? *J. Mater. Chem. B* **2019**, *7*, 5412–5422. [[CrossRef](#)]

71. Bano, D.; Kumar, V.; Singh, V.K.; Chandra, S.; Singh, D.K.; Yadav, P.K.; Talat, M.; Hasan, S.H. A Facile and Simple Strategy for the Synthesis of Label Free Carbon Quantum Dots from the Latex of Euphorbia Milii and Its Peroxidase-Mimic Activity for the Naked Eye Detection of Glutathione in a Human Blood Serum. *ACS Sustain. Chem. Eng.* **2019**, *7*, 1923–1932. [[CrossRef](#)]
72. Lin, Y.; Ren, J.; Qu, X. Nano-Gold as Artificial Enzymes: Hidden Talents. *Adv. Mater.* **2014**, *26*, 4200–4217. [[CrossRef](#)] [[PubMed](#)]
73. Wang, X.; Han, Q.; Cai, S.; Wang, T.; Qi, C.; Yang, R.; Wang, C. Excellent Peroxidase Mimicking Property of CuO/Pt Nanocomposites and Their Application as an Ascorbic Acid Sensor. *Analyst* **2017**, *142*, 2500–2506. [[CrossRef](#)] [[PubMed](#)]
74. Liu, H.; Ding, Y.; Yang, B.; Liu, Z.; Liu, Q.; Zhang, X. Colorimetric and Ultrasensitive Detection of H<sub>2</sub>O<sub>2</sub> Based on Au/Co<sub>3</sub>O<sub>4</sub>-CeOx Nanocomposites with Enhanced Peroxidase-like Performance. *Sens. Actuators B Chem.* **2018**, *271*, 336–345. [[CrossRef](#)]
75. Chen, T.M.; Wu, X.J.; Wang, J.X.; Yang, G.W. WSe<sub>2</sub> Few Layers with Enzyme Mimic Activity for High-Sensitive and High-Selective Visual Detection of Glucose. *Nanoscale* **2017**, *9*, 11806–11813. [[CrossRef](#)]
76. Zheng, H.Q.; Liu, C.Y.; Zeng, X.Y.; Chen, J.; Lü, J.; Lin, R.G.; Cao, R.; Lin, Z.J.; Su, J.W. MOF-808: A Metal-Organic Framework with Intrinsic Peroxidase-Like Catalytic Activity at Neutral PH for Colorimetric Biosensing. *Inorg. Chem.* **2018**, *57*, 9096–9104. [[CrossRef](#)]
77. Zhang, J.W.; Zhang, H.T.; Du, Z.Y.; Wang, X.; Yu, S.H.; Jiang, H.L. Water-Stable Metal-Organic Frameworks with Intrinsic Peroxidase-like Catalytic Activity as a Colorimetric Biosensing Platform. *Chem. Commun.* **2014**, *50*, 1092–1094. [[CrossRef](#)] [[PubMed](#)]
78. Ai, L.; Li, L.; Zhang, C.; Fu, J.; Jiang, J. MIL-53(Fe): A Metal-Organic Framework with Intrinsic Peroxidase-like Catalytic Activity for Colorimetric Biosensing. *Chem. A Eur. J.* **2013**, *19*, 15105–15108. [[CrossRef](#)]
79. Wang, Z.; Liu, J.; Liang, Q.; Wang, Y.; Luo, G. Carbon Nanotube-Modified Electrodes for the Simultaneous Determination of Dopamine and Ascorbic Acid. *Analyst* **2002**, *127*, 653–658. [[CrossRef](#)]
80. Alizadeh, N.; Ghasemi, F.; Salimi, A.; Hallaj, R.; Fathi, F.; Soleimani, F. Polymer Nanocomposite Film for Dual Colorimetric and Fluorescent Ascorbic Acid Detection Integrated Single-Cell Bioimaging with Droplet Microfluidic Platform. *Dye. Pigment.* **2020**, *173*, 107875. [[CrossRef](#)]
81. Ferreira, D.C.M.; Giordano, G.F.; Soares, C.C.D.S.P.; De Oliveira, J.F.A.; Mendes, R.K.; Piazzetta, M.H.; Gobbi, A.L.; Cardoso, M.B. Optical Paper-Based Sensor for Ascorbic Acid Quantification Using Silver Nanoparticles. *Talanta* **2015**, *141*, 188–194. [[CrossRef](#)]
82. Li, R.; An, H.; Huang, W.; He, Y. Molybdenum Oxide Nanosheets Meet Ascorbic Acid: Tunable Surface Plasmon Resonance and Visual Colorimetric Detection at Room Temperature. *Sens. Actuators B Chem.* **2018**, *259*, 59–63. [[CrossRef](#)]

**Disclaimer/Publisher's Note:** The statements, opinions and data contained in all publications are solely those of the individual author(s) and contributor(s) and not of MDPI and/or the editor(s). MDPI and/or the editor(s) disclaim responsibility for any injury to people or property resulting from any ideas, methods, instructions or products referred to in the content.